ADVANCED MATERIALS
www.advmat.de

Acoustically Enhanced Triboelectric Stethoscope for Ultrasensitive Cardiac Sounds Sensing and Disease Diagnosis

Xindan Hui, Lirong Tang, Dewen Zhang, Shanlin Yan, Dongxiao Li, Jie Chen, Fei Wu, Zhong Lin Wang,* and Hengyu Guo**

Electronic stethoscope used to detect cardiac sounds that contain essential clinical information is a primary tool for diagnosis of various cardiac disorders. However, the linear electromechanical constitutive relation makes conventional piezoelectric sensors rather ineffective to detect low-intensity, low-frequency heart acoustic signal without the assistance of complex filtering and amplification circuits. Herein, it is found that triboelectric sensor features superior advantages over piezoelectric one for microquantity sensing originated from the fast saturated constitutive characteristic. As a result, the triboelectric sensor shows ultrahigh sensitivity (1215 mV Pa^{-1}) than the piezoelectric counterpart (21 mV Pa^{-1}) in the sound pressure range of 50–80 dB under the same testing condition. By designing a trumpet-shaped auscultatory cavity with a power function cross-section to achieve acoustic energy converging and impedance matching, triboelectric stethoscope delivers 36 dB signal-to-noise ratio for human test (2.3 times of that for piezoelectric one). Further combining with machine learning, five cardiac states can be diagnosed at 97% accuracy. In general, the triboelectric sensor is distinctly unique in basic mechanism, provides a novel design concept for sensing micromechanical quantities, and presents significant potential for application in cardiac sounds sensing and disease diagnosis.

1. Introduction

Low-intensity and low-frequency (20–600 Hz) cardiac sounds provide essential clinical information for the identification and diagnosis of various heart diseases.[1–5] Currently, electronic stethoscope, a noninvasive instrument of diagnosing cardiac disorders by acquiring the acoustic signal during heart contraction, plays an irreplaceable role for the initial assessment in medical field and personal health management.[5–8] The sensitivity and signal perceptual fidelity of the stethoscope are determined by the rational acoustic and electronic design, their economic costs and popularity. Due to space limitations in the internal acoustic design of the stethoscope, the combined design of a good sound energy focusing structure and efficient electromechanical conversion units becomes even more crucial. Among numerous sensing mechanisms,[9–15] piezoelectric sensors have been widely employed owing to its simple structure, high consistency, and self-powered features.[2,16–19] However, without the assistance of complex filtering and amplification circuits, conventional piezoelectric stethoscope fails to realize the high sensitivity on detecting the heart acoustic signal for the following aspects. On one hand, piezoelectric unit holds the linear electromechanical constitutive relation,[20–23] in this case, tiny deformation induced by low-intensity acoustic stimuli leads to a small output magnitude especially in the pressure range for medical purpose. On the other hand, addressing the need for responsiveness to low-frequency cardiac sounds necessitate mechanical flexibility in the piezoelectric membrane. However, achieving such flexibility comes at the expense of piezoelectric coefficients. This inherent trade-off underscores the challenges faced by conventional piezoelectric stethoscopes in effectively capturing low-frequency heart acoustic signals. Therefore,

X. Hui, L. Tang, D. Zhang, S. Yan, F. Wu, H. Guo
College of Mechanical and Vehicle Engineering
Chongqing University
Chongqing 400044, China
E-mail: wufeifrank@cqu.edu.cn; physghy@cqu.edu.cn

X. Hui, L. Tang, H. Guo
School of Physics
Chongqing University
Chongqing 400044, China

The ORCID identification number(s) for the author(s) of this article can be found under https://doi.org/10.1002/adma.202401508

DOI: 10.1002/adma.202401508

D. Li
Department of Electrical and Computer Engineering
National University of Singapore
Singapore 117583, Singapore

J. Chen
College of Physics and Electronic Engineering
Chongqing Normal University
Chongqing 401331, China

Z. L. Wang
Beijing Institute of Nanoenergy and Nanosystems
Chinese Academy of Sciences
Beijing 100083, China
E-mail: zhong.wang@mse.gatech.edu

new mechanism that is piezoelectric-superior for perceiving both low-intensity and low-frequency heart acoustic signal is highly desired.

Recently, a cutting-edge electromechanical conversion technology based on the coupling effect of contact-electrification (CE) and electrostatic induction, known as triboelectric nanogenerator (TENG), has been proposed for energy harvesting and self-powered sensing.[24–29] TENGs, benefiting from abundant materials choices, have been designed for perceiving various physiological information, including sphygmus,[30–33] eye blinking,[34,35] muscle stretching,[36–39] respiration,[40,41] and in vivo activity.[42,43] Despite the diminutive nature of the sensing targets, TENGs exhibit great advantages to piezoelectric devices, particularly in electric signal level and sensitivity. This characteristic would hold great potential for detecting low-intensity mechanical quantities, such as cardiac sounds. More importantly, a systematical and substantial comparison between these two technologies is still absent, which hinders us to clearly identify the dominant application field and future design direction of triboelectric sensors.

Herein, we carry out a systematical investigation on the electromechanical output character of a contact-separation mode (C-S) TENG and a piezoelectric generator (PEG) and propose that triboelectric sensor features superior advantage over its piezoelectric counterpart in sensing low-intensity and low-frequency cardiac sounds, supported by the following key observations. First, the electric output of TENG shows a fast saturated constitutive characteristic with the increased deformation. This saturation effect becomes even faster when the tribolayer is thinner. In this case, even tiny deformations can be converted into a high electric output, ensuring high sensitivity to low-intensity mechanical quantities. Second, different from piezoelectric device, the direct perceptual layer and electromechanical conversion unit in TENG are relatively independent. In this way, TENG provides a more flexible designability to optimally couple the low-frequency mechanical information without sacrificing its electromechanical coefficient, further improving the sensitivity in cardiac sound sensing. Under the same testing condition, the sensitivity of triboelectric sensor reaches 1215 mV Pa^{-1} in the sound pressure range of 50–80 dB, which is 60 times higher than that of piezoelectric sensor (21 mV Pa^{-1}). To further enhance the performance of the triboelectric stethoscope, a power-law-shaped auscultatory cavity was designed to improve the acoustic impedance matching and acoustic energy converging. By optimizing the structural parameter of the cavity, triboelectric stethoscope delivers 2.3 times higher signal-to-noise ratio (SNR) (36 dB) than piezoelectricity (16 dB) in real human test. Finally, through the integration of machine learning, five cardiac states can be diagnosed with 97% accuracy, which presents the significant potential of TENG technology for application in cardiac sounds sensing and disease diagnosis.

2. Results

2.1. Triboelectric Stethoscope Design and Mechanism

Electronic stethoscope holds paramount significance in medical field, as its performance directly influences the accuracy of heart sounds detection and disease diagnosis. As schematically illustrated in **Figure** 1a, a triboelectric stethoscope is placed on the human chest to record the mechanical acoustic signal during heart beating. The explosion diagram provides an insight to the inner structure of the designed instrument, mainly consisting of an auscultatory cavity and a triboelectric acoustic senor (TAS). As the core electromechanical conversion component of the stethoscope, TAS is prepared by assembling a fluorinated ethylene propylene (FEP) covered with top Al sheet (with multiple apertures), a gap-created spacer and a polyimide (PI) membrane sputtered by gold layer. To enhance the surface charge density, nanostructures are created on the FEP surface by inductive coupled plasma (ICP) etching [44–45] (Inset 1). The detailed fabrication process is delineated in the Experimental Section and Figure S1 (Supporting Information). Here, an auscultatory cavity with inner acoustic structure is further designed to converge the sound energy (Figure 1b), which improves the ability for detecting faint heart sounds. Figure S2 (Supporting Information) displays the simulated sound pressure level (SPL) distribution using this cavity structure. The optical photograph of the triboelectric stethoscope is exhibited in Figure 1c. It is worth noting that, the electromechanical conversion unit is easy to be replaced by other mechanisms (such as PEG), which provides a direct comparison under the same condition (Figure S3a, Supporting Information). Figure 1d illustrates the electrical signal generation mechanism of triboelectric sensor, including the charge transfer schematic (left) and the potential distribution by finite element simulation (right). Typically, PI membrane reciprocally vibrates and contacts with FEP film in response to the acoustic stimuli, inducing negative charges on FEP surface. Consequently, in state I, acoustic pressure propels PI membrane close to the FEP film, causing electrons to flow from Au electrode to Al electrode due to electrostatic induction. In state II, as the PI membrane moves away from the FEP film, electrons flow back to the Au electrode. Above process generates an alternative electrical signal in the external circuit. Contrastively, the electrical output of piezoelectric sensor is originated from the material deformation induced inner dipolarity variation, as depicted in Figure S3b (Supporting Information). Due to the different intrinsic mechanisms, triboelectric and piezoelectric sensor are expected to exhibit distinct performance for cardiac sound sensing. By alternating the electromechanical unit in Figure 1c, the cardiac acoustic signal of a single person is recorded in real time using both triboelectric and piezoelectric stethoscope, as presented in Figure 1e. The electrical signal magnitude and SNR of the triboelectric device reach ≈90 mV and 36 dB, respectively. These values are 50 and 2.3 times higher than those of piezoelectric one (≈2 mV, 16 dB), and 2 and 1.8 times higher than those of a commercial instrument (≈45 mV, 20 dB) (CM-01B) with a filtering and amplification module (Figure S4, Supporting Information). Table S1 (Supporting Information) summarizes the basic characteristics of TENG, PEG, and commercial heart sound sensor. This outcome underscores the superior advantage of TENG in detecting low-intensity and low-frequency heart sounds.

2.2. Fundamental Comparison of TENG and PEG on Electromechanical Conversion

To reveal the reasons behind the advantages exhibited by TENG and identify potential applications where it can replace a PEG, a

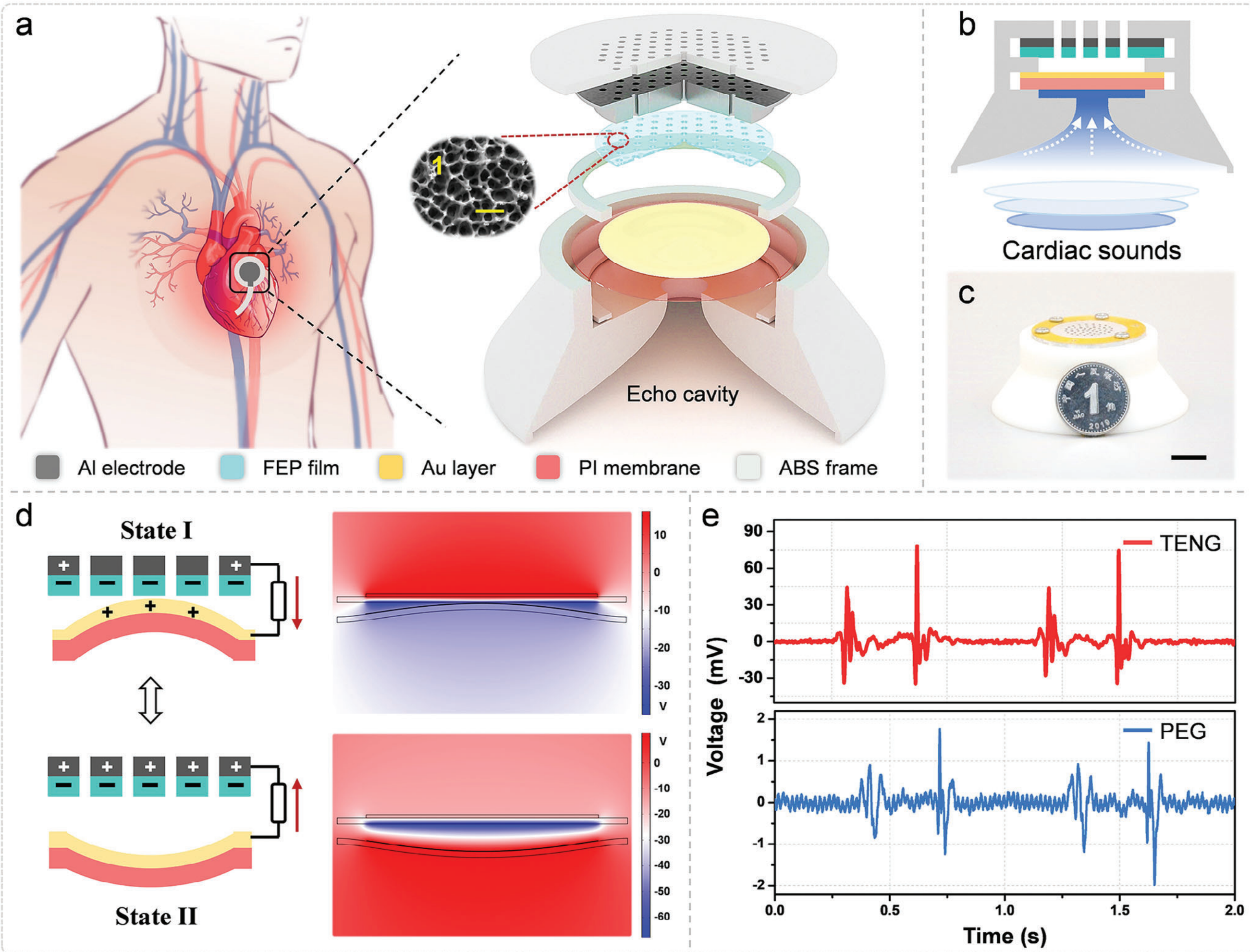

Figure 1. Structure and sensing mechanism of the triboelectric stethoscope. a) Schematic illustration of cardiac sounds sensing using the triboelectric stethoscope and exploded view diagram of the overall design structure. Inset 1: The surface morphology of the tribolayer (scale bar: 1 µm). b) Cross-sectional diagram of the device and capability for cardiac sounds converging. c) Optical photograph of the triboelectric stethoscope with a coin for size comparison (scale bar: 10 mm). d) Charge (Left) and simulated potential (Right) distribution of triboelectric unit in two typical states under short- and open-circuit condition, respectively. e) Output electrical signal comparison of triboelectric and piezoelectric stethoscope for real body test.

systematical comparison on their electromechanical constitutive relation is the most fundamental and significant aspect. In this regard, both a C-S TENG and a one-end-fixed cantilever-based PEG are used for theoretical and experimental investigations, as structural schematic shown in **Figure 2**a,b (left). In the presence of mechanical force, a certain displacement D is applied directly on the top layer of TENG and the free-end of PEG, respectively. Considering the actual test condition of TENG, the output voltage and charge can be derived as (Note S1, Supporting Information)

$$V_{TENG} = \frac{S\sigma}{\frac{C_0 \cdot d_0 + \epsilon_0 \cdot S}{D} + C_0} \tag{1}$$

$$Q_{TENG} = \frac{S\sigma}{d_0 + D} \cdot D \tag{2}$$

where S, σ, and d_0 denote the area size, surface charge density, and effective thickness ($d_0 = T/\epsilon_{r1}$, T is the thickness marked in Figure 2a, ϵ_{r1} is the relative dielectric constant) of the tribolayer, respectively. C_0 represents the equivalent extra capacitance in the whole testing system. For the cantilever-based PEG (Figure 2b), the piezoelectric effect primarily correlates with the deformation of the material in the thickness direction, specifically involving the d_{31} piezoelectric constant. Consequently, the output voltage and charge can be expressed as (Note S2, Supporting Information)

$$V_{PEG} = \frac{3d_{31}\pi kET^2}{2L^2\epsilon_{r2}} \cdot D \tag{3}$$

$$Q_{PEG} = \frac{3d_{31}EwT}{8L} \cdot D \tag{4}$$

where L, w, and T are the length, width, and thickness of the cantilever beam, respectively. k is the coulomb constant, while E and ϵ_{r2} represent Young's modulus and relative dielectric

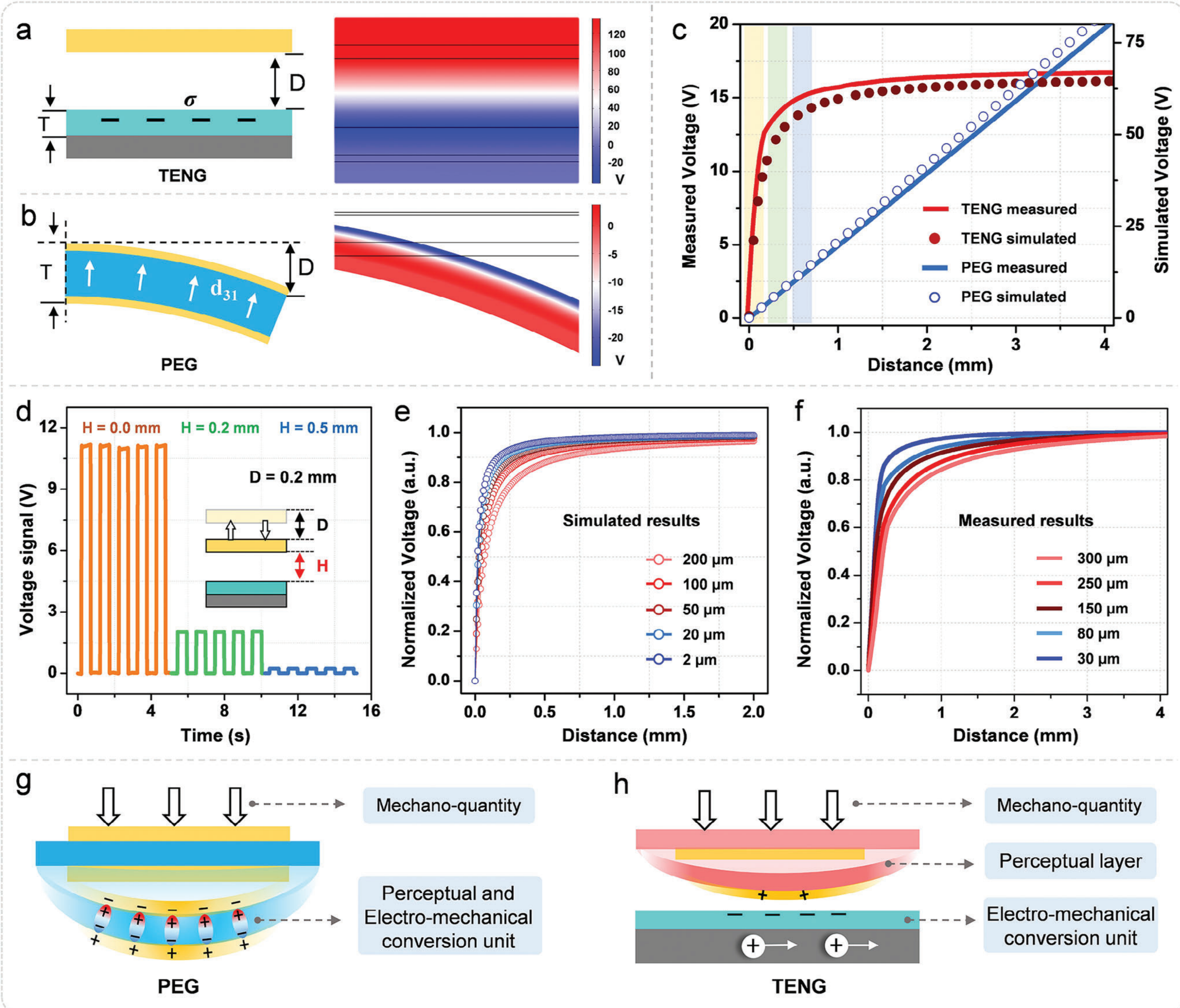

Figure 2. Comparison of TENG and PEG on electromechanical conversion. a,b) Schematic diagram of the working principle (left) and simulated potential (right) distribution of contact-separation mode TENG and cantilever beam PEG, respectively. c) The voltage output of TENG and PEG versus displacement. d) Output voltage signal of TENG at three specific initial distance (shadow area in (c)). e,f) The simulated and measured normalized output voltage of TENG with various tribolayer thickness. Schematic illustration of the coupling mode between mechanical quantity, device, and electric output of g) TENG and h) PEG.

constant of the piezoelectric material, respectively. Furthermore, the output of TENG and PEG can also be simulated by finite element method (left of Figure 2a,b). Experimentally, the output voltage and charge versus the displacement are measured using the setup in Figure S5 (Supporting Information). As plotted in Figure 2c and Figure S6 (Supporting Information), distinguished from the linear constitutive relation of PEG, C-S TENG demonstrates a fast saturated output characteristic over displacement. This distinctive feature indicates that the output of TENG would be significantly higher than that of PEG when the displacement is minute (yellow back area), indicating a high sensitivity for micromechanical quantity sensing. Nevertheless, for a given microdisplacement (ΔD), the initial gap (H) between top electrode and tribolayer plays a pivotal role in the output of TENG (green and blue back area in Figure 2c). As shown in Figure 2d, with the fixed ΔD (0.2 mm), the output voltage experiences a rapid decline as H increases from 0 to 0.5 mm. Hence, an optimized initial state is also important for triboelectric sensor. According to Equations (1)–(4), under a fixed ΔD, optimizing output of the device involves increasing surface charge density and reducing the material thickness for TENG. While, for PEG, enhancing the output necessitates an increase in the piezoelectric coefficient and material thickness. Figure 2e,f presents the simulated and measured normalized voltage–displacement relation (charge–displacement are depicted in Figure S7, Supporting Information) with various tribolayer thicknesses, respectively. The results exhibit that a thinner tribolayer leads to a faster saturation effect in TENG device, rendering it more efficient for microdisplacement region.

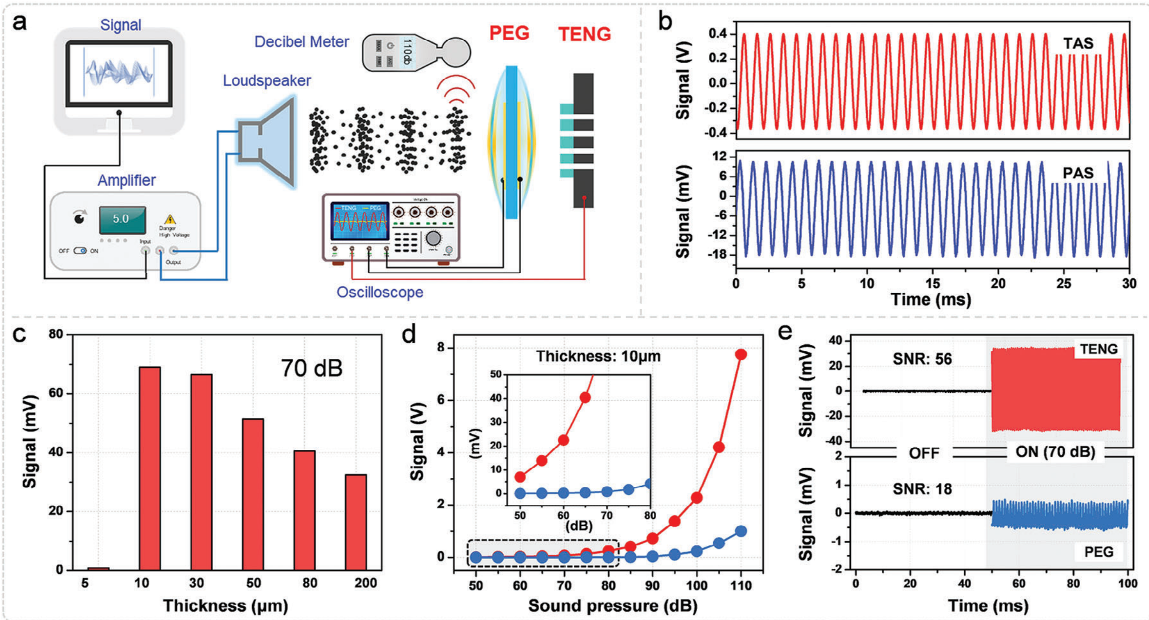

Figure 3. Performance comparison between triboelectric (TAS) and piezoelectric (PAS) acoustic sensor. a) Schematic illustration of the setup for simultaneously testing TAS and PAS. b) Output signal of TAS and PAS. c) The influence of tribolayer thickness on the output signal of TAS at 70 dB. d) The acoustic response of TAS and PAS under various sound intensities. e) Acoustic response difference between the noise and specific sound signal of TAS and PAS.

In addition, the coupling mode between mechanical quantity, device, and electric output of TENG differ from those in PEG. As illustrated in Figure 2g, for PEG, the piezoelectric material functions as both mechanosensitive layer and electromechanical conversion element. The magnitude of the electric output highly depends on the piezoelectric coefficient and the deformation amplitude. Typically, high coefficient piezoelectric materials are most ceramic and rigid, which fail to efficiently couple the low-intensity and low-frequency physical quantities, while piezoelectric coefficient of flexible piezoelectric polymers is an order of magnitude lower than that of ceramic material. Therefore, PEG operates with a strong coupling mode, and its performance for a given mechanical quantity cannot be improved from one a single aspect. Otherwise, for TENG (Figure 2h), mechanical quantity applies on the top perceptual layer independently, the created deformation then induces electric output cooperatively with bottom tribolayer. In this scenario, the perceptual layer can be flexibly selected and designed, allowing for enhanced electric output by increasing the surface charge density and reducing the thickness of tribolayer. Table S2 (Supporting Information) summarizes the basic characteristics of TENG and PEG for electromechanical conversion. In general, the rapidly saturated constitutive relation and relatively independent mechanosensitive and electromechanical conversion elements confer upon TENG the superior advantage over PEG on cardiac sound sensing.

2.3. Performance Comparison between Acoustic Sensors Based on TENG and PEG

To highlight the feature of triboelectric stethoscope, acoustic tests are conducted to compare the performance of TENG and PEG synchronously. The polarized PVDF film (purchased from TE Connectivity Inc.) with Au electrodes sputtered on the upper and lower surfaces serves as both the piezoelectric acoustic sensor (PAS) and the top perceptual membrane of the triboelectric acoustic sensor (TAS), as depicted in **Figure 3**a. The corresponding experimental setup is shown in Figure S8 (Supporting Information). Figure 2c,d indicates that the initial distance between the top and bottom layer exerts notable influence on the output of TAS. The bottom Al sheet is fixed on a 3D stage, enabling precise adjustment of the distance until TENG output reaches its maximum value (Figure S9, Supporting Information). Using this experimental platform, TAS and PAS hold the same frequency response characteristic (Figure S10, Supporting Information), which ensures the identical comparability. Figure 3b displays the electric signals of the two sensors under the resonance frequency (1145 Hz) and a sound pressure level (SPL) of 85 dB, revealing a significantly higher signal obtained by TAS. Moreover, in accordance with Equations (1) and (2) and Figure 2e,f, maintaining a constant surface charge density enables further enhancement of the output of TAS by diminishing the thickness of tribolayer. To control the surface charge density, an air ion gun is utilized to inject a constant charge quantity onto FEP surface with various thicknesses.[46] As illustrated in Figure 3c, a higher output voltage results in a thinner FEP film, reaching its peak at10 µm. However, as the thickness of tribolayer is further reduced to 5 µm, a rapid decline in output voltage is observed. This phenomenon may be attributed to the inner charge diffusion and tunneling effects of the electret film (Figure S11 and Note S3, Supporting Information), marking a pivotal consideration for elevating TAS sensitivity in future developments. Consequently, the 10 µm FEP is chosen for further assessment of the output amplitudes of TAS and PAS under the resonance frequencies and SPLs ranging from 50

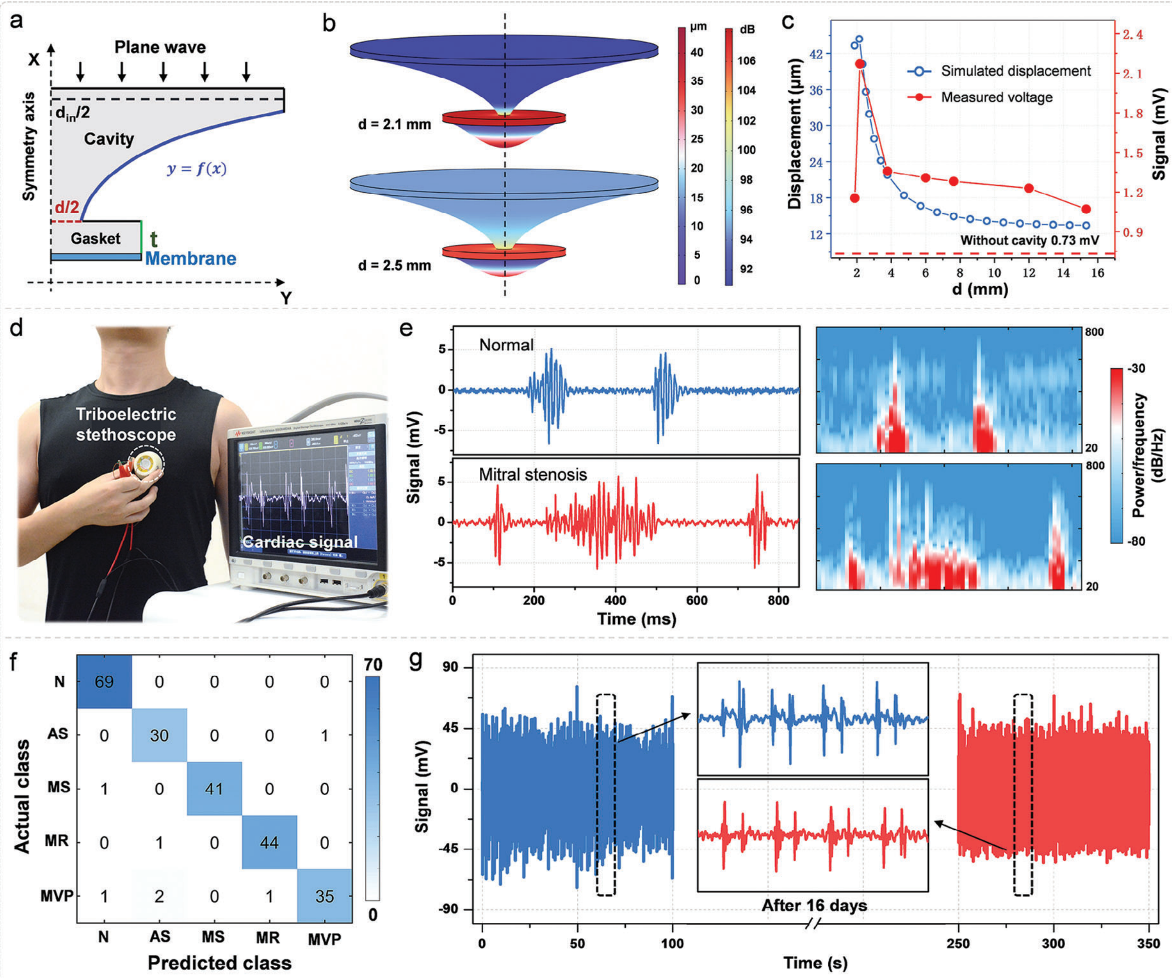

Figure 4. Auscultatory cavity design and application demonstration of triboelectric stethoscope. a) The 2D symmetric diagram of the cavity. b) Simulated sound pressure level distribution and membrane vibration displacement for two typical cavities. c) Simulated membrane vibration displacement and measured output signal using the cavity with various aperture diameter. d) Photograph of using a triboelectric stethoscope to detect cardiac sounds and corresponding electrical signals. e) Time-series plot of cardiac sounds for normal and mitral stenosis (left) and the corresponding spectrograms (right). f) The confusion matrix for the five triggers. g) Long-term stability of triboelectric stethoscope after 16 d. The insets show the magnified detailed cardiac sounds.

to 110 dB (Figure 3d). In the weak acoustic of 50–80 dB, PAS exhibits diminutive output with a sensitivity of ≈21 mV Pa^{-1}, whereas TAS maintains significant output with an impressive sensitivity of ≈1215 mV Pa^{-1} (Figure S12, Supporting Information). This exceptional performance is also reflected in the SNR under low-intensity stimuli. As shown in Figure 3e, TAS attains a 56 dB SNR, surpassing PAS by 3.1 times (18 dB), when the SPL is 70 dB. All above demonstrate the superior advantage of TAS over PAS for low-intensity acoustic wave detection particularly in cardiac sounds.

2.4. Triboelectric Stethoscope for Cardiac Sounds Sensing and Disease Diagnosis

In order to facilitate the detection of human heart sounds through TAS, an acoustic resonant system has been created by incorporating TAS, an auscultatory cavity, and a gasket. This system is designed to efficiently convert acoustic energy and isolate external noise. A trumpet-shaped cavity (auscultatory cavity) with a power-law cross-section is carefully designed, thus, the incident sound waves drive a mass of air within the cavity, initiating a reciprocating motion, while being subjected to the elastic restorative force of the TAS membrane. By drilling holes in the ABS frame, when the film is vibrated, the air in the back can be discharged through the holes to equalize the pressure difference between the inside and outside. The perforated plate allows the remaining air cavity to not additionally increase the total elastic stiffness of the system, which is favorable to the intrinsic frequency to be more low-frequency. **Figure 4a** presents the sectional symmetric schematic diagram of the cavity. The conventional exponential horn tube structure improves sensor collar sensitivity but has a cutoff frequency.[47] Acoustic waveguide-type acoustic black holes are composed using a ring whose radius decreases to zero according to a power function change [48] with a slow acoustic effect that makes acoustic energy converge. The inner shell structure is designed using the power function curve [49]: $y = \mu x^n + y_0$, (n = 3, 4 ⋯, $x \in [x_1, x_2]$, $\mu = (d_{in} - y_0)/(x_2^n)$, x representing the argument along the axis of symmetry; $x_1 = 5$ mm, $x_2 = 15$ mm; y_0 being the curve offset compensation value; d_{in} indicating the diameter of the incoming port; μ is used as a curve compensation factor to control the constant incident port diameter d_{in}) which has the effective capability for acoustic energy converging, as depicted in Figure S13a (Supporting Information). For a curve, when d_{in} is given, its function is determined by the power term n and the curve offset compensation y_0. These two parameters affect the surface curvature of the cavity and the diameter of the output port d , thereby influencing the acoustical characteristics and sound damping of the structure. The simulated SPL and membrane displacement in Figure S13b (Supporting Information) indicate that the optimized curve for low-frequency sound (200 Hz) is obtained when the power factor n equals 3. In addition, the aperture diameter near the gasket plays a critical role on converging of acoustic energy, which further influences the membrane vibration amplitude. Two representative simulated results (d = 2.1 and 2.5 mm) (Figure 4b) indicate the effect of aperture diameter on SPL and membrane displacement. As the quantitative data plotted in Figure 4c and Figure S13c (Supporting Information), the maximum SPL, displacement and measured output for a PAS are yielded by the optimized aperture diameter of 2.1 mm. The impact of gasket thickness on cavity performance is presented in Figure S13d (Supporting Information). With the increase in the thickness of the gasket, the gap region between the membrane and the small hole enlarges. This initially leads to a decrease in SPL, but it eventually increases to a stable value. Meanwhile, the membrane displacement rapidly increases to its maximum and gradually decreases. Based on the above analysis, the optimized auscultator cavity is prepared with the power factor of 3, aperture diameter of 2.1 mm, and gasket thickness of 0.5 mm. Figure S13e,f (Supporting Information) illustrates the frequency selectivity of the cavity, indicating that the primary response frequencies are predominantly concentrated in the lower frequency spectrum, aligning well with the frequency range of cardiac sounds (20–600 Hz). This feature would effectively avoid cardiac signal distortion, shield external acoustic noise interference, thus further enhance the performance and reliability of the stethoscope. Figure 4d demonstrates the application of TAS in a human body test. Videos S1 and S2 (Supporting Information) dynamically display the assembly and testing procedures of TAS and PAS. The converted electric signals are recorded by an oscilloscope and transformed to the audio file though a Matlab program. The comparison of the measured cardiac signal for a single person using triboelectric, piezoelectric device and commercial instrument (CM-01B) are recorded in Videos S3–S5 (Supporting Information), respectively. Figure 4e and Figure S14 (Supporting Information) depict the heart sound wave and the spectrogram of five cardiac states, including normal and four typical heart diseases. Different cardiac conditions manifest distinctive frequency characteristics, which is greatly favorable for the introduction of machine learning algorithms to realize intelligent detection and diagnosis of cardiac diseases. In the experiment, a total of 1126 sets of heart sound data are collected, comprising 1000 sets from a dataset and an additional 126 sets gathered from nine subjects. Among these, there are 326 sets for the normal state and 200 sets for each of the four distinct diseases. Figure S15 (Supporting Information) demonstrates the cardiac sounds of the nine participants. To develop our model, 80% of the entire dataset is allocated for training purposes, while the remaining 20% is reserved for prediction. The heart sound data undergoes processing using convolutional neural networks (CNNs), with their structure shown in Figure S16a (Supporting Information). The influence of the training epoch on accuracy and loss in prediction is portrayed in Figure S16b,c (Supporting Information). It is obvious that the accuracy rate increases with the rise of train epochs and stabilizes after 10 epochs. After executing 30 train epochs, the confusion matrix of the classification in Figure 4f reveals a recognition accuracy of 97%. Video S6 (Supporting Information) shows the interface of the point-of-care-testing for the diagnosis of heart conditions. Finally, the long-term stability of the TAS is measured before and after 16 d, as depicted in Figure 4g. Notably, the amplitude of the heart sound signals remains stable, underscoring the robustness and practicability of TAS.

3. Conclusion

In summary, we demonstrated a piezoelectric-superior triboelectric stethoscope for cardiac sound sensing and disease diagnosis. By systematically investigating the electromechanical output characteristics of C-S TENG and PEG, the fast saturated constitutive characteristic and the relatively independent mechanoperception and electromechanical conversion component emerge as key factors contributing to the superior performance of TENG over PEG in the detection of low-intensity and low-frequency cardiac sounds. Experimentally, TAS demonstrates the sensitivity of 1215 mV Pa^{-1} and SNR of 56 dB, outperforming its piezoelectric counterpart (21 mV Pa^{-1}, 18 dB) under the low-intensity acoustic stimuli by 60 and 3.1 times, respectively. Leveraging machine learning algorithms, we constructed a point-of-care-testing interface to intelligently identify and diagnose five heart conditions with 97% accuracy. This work shows a key application field and future design direction of triboelectric sensors, involving subtle vibration, human physiological signal, and underwater acoustic communication et al. In addition, this novel triboelectric stethoscope enables the ultrasensitive and self-powered for heart sound detection, thereby enhancing the accuracy of disease identification. Future studies will focus on the improvement of SNR, the consistency of triboelectric components and the engineering of heart sound detection system with the overarching goal of advancing their clinical integration within medical science and contributing to the evolution of sophisticated intelligent medical equipment.

4. Experimental Section

Numerical Simulation: The potential distribution of TENG and PEG and parameters optimization of auscultatory cavity were numerically calculated using a commercial software COMSOL Multiphysics (6.0 version). To save simulation time and boost the modeling efficiency, a 2D model and 2D axisymmetric model were used for simulation. Table S3 (Supporting Information) summarizes the basic simulation settings of TENG and PEG for electromechanical conversion.

Fabrication of TAS: An aluminum sheet (thickness, 5 mm) was cut into circular pieces (diameters, 30 and 15 mm) with multiple holes (diameter, 0.8 mm) to act as the upper electrode by milling machine (CNC

4030, JingYan Instruments & Technology Co., Ltd.). Perforated structure effectively reduces air damping and enhance acoustic energy utilization. A metallographic polishing machine (Fpol 252A pro, Suzhou FEMA Testtech Co., Ltd) was used to grind and polish the surface of circular pieces for spin-coating and adhering triboelectric layer. Here, oily FEP solution and FEP film (purchased from Taobao Inc.) were used. A spin coater (IC8000-S, Jiangsu Lebo Science Inc.) was used to prepare ultrathin FEP film, and the thickness was characterized by an optical film thickness meter (Wuhan EOptics Technology Co., Ltd.). To enhance the surface charge density, inductively coupled plasma reactive-ion etching was used to create nanostructure on the FEP surface. Afterward, a PI film (thickness, 6 µm) covered with Au layer was adhered on the annular aluminum piece (outer diameter, 30 mm and inner diameter, 22 mm) as the vibration membrane and worked as the bottom electrode. Finally, screws (diameter, 2 mm, length, 6 mm) were used to fix the edges of the upper and lower electrodes and regulate the gap between them.

Electric Measurement and Characterization: Field-emission scanning electron microscopy (Hitachi SU8010) was used to characterize the surface morphology of the nanostructured FEP film. Power amplifier (Aigtek ATA-304B) was used to amplify audio signals to drive loudspeaker. The electrical signals were recorded using a programmable electrometer (Keithley 6514) and oscilloscope (Keysight infiniiVision DSOX4024A). A sound meter (UT353 BT, Uni-Trend Technology Co., Ltd.) was used to characterize the SPL.

Collection of Sound Data: The stethoscope was mounted on mitral area point of subjects for collecting cardiac sounds. The duration for each recording heart sounds was 5 s. Testing subjects were asked to do different activities under breathing and breath-holding, including standing, lying down, sitting, and exercising. From nine subjects, 126 sets of normal heart sounds data were obtained, and the remaining one thousand sets of data were acquired from the open-source dataset provided by Yaseen in 2018. The heart sounds of dataset were played at 50 dB, and collected by the TAS to simulate a real human test.

Classification of Heart Sounds: Heart sounds were collected with the same data length (16 000 sampling points). For training, second-order spectral analysis was used to obtain grayscale maps of the same size for feature extraction. Then, these data were entered into a CNN, featuring four layers of 2D convolutions with filters of size (32, 16, and 8, respectively). Each convolutional layer was followed by batch normalization and max-pooling step with a filter size of 2. Finally, the data were followed by a fully connected layer and Softmax output. The network variables were optimized using the Adam optimization algorithm.

Statistical Analysis: MATLAB (2020a version) was used to analyze measured signals. Before employing machine learning, the signal processing involved a wavelet denoising algorithm (waveletname = db10, level = 5, soft-threshold) and a Butterworth bandpass filter (20–600 Hz). The data were normalized by dividing by the maximum value.

Calculation of the Sensitivity: The relationship between sound pressure and sound pressure level was expressed as

$$\mathrm{SPL} = 20\lg\frac{P}{P_0} \tag{5}$$

where P is the sound pressure, and P_0 is the reference sound pressure of 2×10^{-5} Pa.

According to the above equation, the relation between different sound pressure and output voltage of sensor was obtained (Figure S12, Supporting Information). The Origin software (2017, version) was used for linear fitting, and the slope as the sensitivity.

Calculation of the SNR: The SNR of the sensor was calculated by

$$\mathrm{SNR} = 20\log_{10}\left(\frac{V_{\mathrm{signal}}}{V_{\mathrm{noise}}}\right) \tag{6}$$

where V_{signal} is the peak output voltage of the sensor, and V_{noise} is the peak output voltage of the noise; the SNR is expressed in dB.

Statement: Participants took part in experiments described herein with informed consent, and no formal approval from these experiments was required.

Supporting Information

Supporting Information is available from the Wiley Online Library or from the author.

Acknowledgements

This work was financially supported by the NSFC (U21A20147 and 52302219), the National Key Research and Development Program (2021YFA1201602), the Postdoctoral Science Foundation (2023M730419), and the Fundamental Research Funds for the Central Universities (Grant No. 2024CDTZCQ-012).

Conflict of Interest

The authors declare no conflict of interest.

Author Contributions

X.H., L.T., and D.Z. contributed equally to this work. X.H. and H.G. conceived the idea. F.W., H.G., and Z.L.W. supervised the project. X.H. and L.T. designed the experiment part, completed the electrical performance measurement part, and wrote the original draft. D.L., D.Z., and S.Y. were responsible for the numerical simulation. H.G., J.C., and Z.L.W. revised the manuscript. J.C. and F.W. provided some advice. All authors contributed to the paper.

Data Availability Statement

The data that support the findings of this study are available from the corresponding author upon reasonable request.

Keywords

cardiac disorder, electronic stethoscope, low-intensity cardiac signal, piezoelectric, triboelectric

Received: January 29, 2024
Revised: May 2, 2024
Published online: May 20, 2024

[1] M. O. G. Nayeem, S. Lee, H. Jin, N. Matsuhisa, H. Jinno, A. Miyamoto, T. Yokota, T. Someya, *Proc. Natl. Acad. Sci. USA.* **2020**, *117*, 7063.
[2] J. Zang, C. Zhou, M. Xiang, J. Wang, H. Wang, Z. Zhang, C. Xue, *Adv. Mater. Technol.* **2022**, *7*, 2101501.
[3] Y. Liu, M. Pharr, G. A. Salvatore, *ACS Nano.* **2017**, *11*, 9614.
[4] Y. Li, Y. Huang, N. Zhao, *Adv. Funct. Mater.* **2023**, *33*, 2300666.
[5] S. H. Lee, Y.-S. Kim, M.-K. Yeo, M. Mahmood, N. Zavanelli, C. Chung, J. Y. Heo, Y. Kim, S.-S. Jung, W.-H. Yeo, *Sci. Adv.* **2022**, *8*, eabo5867.
[6] A. Ramanathan, L. Zhou, F. Marzbanrad, R. Roseby, K. Tan, A. Kevat, A. Malhotra, *Acta Paediatr.* **2019**, *108*, 814.
[7] Y. Kim, Y. Hyon, S. Lee, S.-D. Woo, T. Ha, C. Chung, *BMC Pulm. Med.* **2022**, *22*, 119.

[8] M. E. H. Chowdhury, A. Khandakar, K. Alzoubi, S. Mansoor, A. M. Tahir, M. B. I. Reaz, N. Al-Emadi, *Sensors.* **2019**, *19*, 2781.
[9] M. A. Shah, I. A. Shah, D.-G. Lee, S. Hur, *Chuangan Jishu Xuebao.* **2019**, *2019*,9294528.
[10] Y. Liu, J. J. S. Norton, R. Qazi, Z. Zou, K. R. Ammann, H. Liu, L. Yan, P. L. Tran, K.-I. Jang, J. W. Lee, D. Zhang, K. A. Kilian, S. H. Jung, T. Bretl, J. Xiao, M. J. Slepian, Y. Huang, J.-W. Jeong, J. A. Rogers, *Sci. Adv.* **2016**, *2*, e1601185.
[11] K. Lee, X. Ni, J. Y. Lee, H. Arafa, D. J. Pe, S. Xu, R. Avila, M. Irie, J. H. Lee, R. L. Easterlin, D. H. Kim, H. U. Chung, O. O. Olabisi, S. Getaneh, E. Chung, M. Hill, J. Bell, H. Jang, C. Liu, J. B. Park, J. Kim, S. B. Kim, S. Mehta, M. Pharr, A. Tzavelis, J. T. Reeder, I. Huang, Y. Deng, Z. Xie, C. R. Davies, et al., *Nat. Biomed. Eng.* **2019**, *4*, 148.
[12] M. J. Tadi, E. Lehtonen, A. Saraste, J. Tuominen, J. Koskinen, M. Teräs, J. Airaksinen, M. Pänkäälä, T. Koivisto, *Sci. Rep.* **2017**, *7*, 6823.
[13] G. Yilmaz, M. Rapin, D. Pessoa, B. M. Rocha, A. M. d. Sousa, R. Rusconi, P. Carvalho, J. Wacker, R. P. Paiva, O. Chételat, *Sensors.* **2020**, *20*, 5124.
[14] W. Yan, G. Noel, G. Loke, E. Meiklejohn, T. Khudiyev, J. Marion, G. Rui, J. Lin, J. Cherston, A. Sahasrabudhe, J. Wilbert, I. Wicaksono, R. W. Hoyt, A. Missakian, L. Zhu, C. Ma, J. Joannopoulos, Y. Fink, *Nature.* **2022**, *603*, 616.
[15] Y. Cotur, M. Kasimatis, M. Kaisti, S. Olenik, C. Georgiou, F. Güder, *Adv. Funct. Mater.* **2020**, *30*, 1910288.
[16] B. Liu, L. Han, L. Pan, X. Wang, *Sensors.* **2021**, *21*, 4508.
[17] S. Mokhtari, M. A. Ahmad, *Alexandria Eng. J.* **2019**, *58*, 1053.
[18] H. Chen, S. Yu, H. Liu, J. Liu, Y. Xiao, D. Wu, X. Pan, C. Zhou, Y. Lei, S. Liu, *Microsyst. Nanoeng.* **2021**, *7*, 55.
[19] D. Y. Park, D. J. Joe, D. H. Kim, H. Park, J. H. Han, C. K. Jeong, H. Park, J. G. Park, B. Joung, K. J. Lee, *Adv. Mater.* **2017**, *29*, 1702308.
[20] S. Park, X. Guan, Y. Kim, F. P. X. Creighton, E. Wei, I. J. Kymissis, H. H. Nakajima, E. S. Olson, *Trends Hear.* **2018**, *22*, 1.
[21] D. B. Deutz, N. T. Mascarenhas, J. B. J. Schelen, D. M. d. Leeuw, S. van der Zwaag, P. Groen, *Adv. Funct. Mater.* **2017**, *27*, 1700728.
[22] Y. H. Jung, S. K. Hong, H. S. Wang, J. H. Han, T. X. Pham, H. Park, J. Kim, S. Kang, C. D. Yoo, K. J. Lee, *Adv. Mater.* **2019**, *32*, 1904020.
[23] L. Lin, Q. Jing, Y. Zhang, Y. Hu, S. Wang, Y. Bando, R. P. S. Han, Z. L. Wang, *Energy Environ. Sci.* **2013**, *6*, 1164.
[24] X. Wei, B. Wang, X. Cao, H. Zhou, Z. Wu, Z. L. Wang, *Nat. Food.* **2023**, *4*, 721.
[25] W. Xu, H. Zheng, X. Deng, M. Leung, X. C. Zeng, Y. Liu, Z. Wang, X. Zhou, Z. Yang, R. X. Xu, *Nature.* **2020**, *578*, 392.
[26] Q. Shi, Z. Sun, X. Le, J. Xie, C. Lee, *ACS Nano.* **2023**, *17*, 4985.
[27] D. Choi, Y. Lee, Z.-H. Lin, S. Cho, M. Kim, C. K. Ao, S. Soh, C. Sohn, C. K. Jeong, J. Lee, M. Lee, S. Lee, J. Ryu, P. Parashar, Y. Cho, J. Ahn, I.-D. Kim, F. Jiang, P. S. Lee, G. Khandelwal, S.-J. Kim, H. S. Kim, H.-C. Song, M. Kim, J. Nah, W. Kim, H. G. Menge, Y. T. Park, W. Xu, J. Hao, et al., *ACS Nano.* **2023**, *17*, 11087.
[28] D.-M. Lee, N. Rubab, I. Hyun, W. Kang, Y.-J. Kim, M. Kang, B. O. Choi, S.-W. Kim, *Sci. Adv.* **2022**, *8*, eabl8423.
[29] D. Jiang, B. Shi, H. Ouyang, Y. Fan, Z. L. Wang, Z. Li, *ACS Nano.* **2020**, *14*, 6436.
[30] X. Wang, J. Yang, K. Meng, Q. He, G. Zhang, Z. Zhou, X. Tan, Z. Feng, C. Sun, J. Yang, Z. L. Wang, *Adv. Funct. Mater.* **2021**, *31*, 2102378.
[31] K. Dong, Z. Wu, J. Deng, A. C. Wang, H. Zou, C. Chen, D. Hu, B. Gu, B. Sun, Z. L. Wang, *Adv. Mater.* **2018**, *30*, 1804944.
[32] H. Ouyang, J. Tian, G. Sun, Y. Zou, Z. Liu, H. Li, L. Zhao, B. Shi, Y. Fan, Y. Fan, Z. L. Wang, Z. Li, *Adv. Mater.* **2017**, *29*, 1703456.
[33] Z. Liu, Z. Zhao, X. Zeng, X. Fu, Y. Hu, *Nano Energy.* **2019**, *59*, 295.
[34] X. Pu, H. Guo, J. Chen, X. Wang, Y. Xi, C. Hu, Z. L. Wang, *Sci. Adv.* **2017**, *3*, e1700694.
[35] Y. Shi, P. Yang, R. Lei, Z. Liu, X. Dong, X. Tao, X. Chu, Z. L. Wang, X. Chen, *Nat. Commun.* **2023**, *14*, 3315.
[36] D. Yang, Y. Ni, X. Kong, S. Li, X. Chen, L. Zhang, Z. L. Wang, *ACS Nano.* **2021**, *15*, 14653.
[37] J. Wang, H. Wang, N. V. Thakor, C. Lee, *ACS Nano.* **2019**, *13*, 3589.
[38] Y. Dong, S. S. K. Mallineni, K. Maleski, H. Behlow, V. N. Mochalin, A. M. Rao, Y. Gogotsi, R. Podila, *Nano Energy.* **2018**, *44*, 103.
[39] F. Yi, L. Lin, S. Niu, P. K. Yang, Z. Wang, J. Chen, Y. Zhou, Y. Zi, J. Wang, Q. Liao, Y. Zhang, Z. L. Wang, *Adv. Funct. Mater.* **2015**, *25*, 3688.
[40] J. Li, Y. Long, F. Yang, X. Wang, *EcoMat.* **2020**, *2*, e12045.
[41] Y. Su, G. Chen, C. Chen, Q. Gong, G. Xie, M. Yao, H. Tai, Y. Jiang, J. Chen, *Adv. Mater.* **2021**, *33*, 2101262.
[42] H. Ryu, H. M. Park, M. K. Kim, B. Kim, H. S. Myoung, T. Y. Kim, H. J. Yoon, S. S. Kwak, J. Kim, T. H. Hwang, E. K. Choi, S. W. Kim, *Nat. Commun.* **2021**, *12*, 4374.
[43] M. Zhou, M. Huang, H. Zhong, C. Xing, Y. An, R. Zhu, Z. Jia, H. Qu, S. Zhu, S. Liu, L. Wang, H. Ma, Z. Qu, G. Ning, S. Feng, *Adv. Funct. Mater.* **2022**, *32*, 2200269.
[44] Y. Zhou, W. Deng, J. Xu, J. Chen, *Cell Rep. Phys. Sci.* **2020**, *1*, 100142.
[45] Y. Zou, J. Xu, K. Chen, J. Chen, *Adv. Mater. Technol.* **2021**, *6*, 2000916.
[46] S. Wang, Y. Xie, S. Niu, L. Lin, C. Liu, Y. S. Zhou, Z. L. Wang, *Adv. Mater.* **2014**, *26*, 6720.
[47] D. J. Mennitt, K. M. Fristrup, B. M. Notaros, *J. Acoust. Soc. Am.* **2017**, *142*, 3257.
[48] A. Pelat, F. Gautier, S. C. Conlon, F. Semperlotti, *J. Sound Vib.* **2020**, *476*, 115316.
[49] Y. Mi, W. Zhai, L. Cheng, C. Xi, X. Yu, *Appl. Phys. Lett.* **2021**, *118*, 114101.